Metasurface-enabled single-shot and complete Mueller matrix imaging

Aun Zaidi [1] ✉, Noah A. Rubin [1,2], Maryna L. Meretska [1,3], Lisa W. Li [1], Ahmed H. Dorrah [1], Joon-Suh Park [1] & Federico Capasso [1] ✉

When light scatters off an object, its polarization, in general, changes—a transformation described by the object's Mueller matrix. Mueller matrix imaging is an important technique in science and technology to image the spatially varying polarization response of an object of interest, to reveal rich information otherwise invisible to traditional imaging. Here we conceptualize, implement and demonstrate a compact Mueller matrix imaging system—composed of a metasurface to produce structured polarization illumination and a metasurface for polarization analysis—that can, in a single shot, acquire all 16 components of an object's spatially varying Mueller matrix over an image. Our implementation, which is free of any moving parts or bulk polarization optics, should enable and empower applications in real-time medical imaging, material characterization, machine vision, target detection and other important areas.

Traditionally, imaging in optics is understood to capture the intensity of a light field. Imaging then usually quantifies an object's spatially varying intensity response under given illumination conditions, providing a simplified description of a more complex light–object interaction. The measurement of optical intensity, being a time-averaged square modulus of the electric field vector, necessarily 'flattens' many degrees of freedom of light and natural scenes. Imaging beyond intensity in a way that can recover a fuller picture of light and light–matter interaction, and the optical hardware to enable this imaging, are overarching goals of research in optics. In what is perhaps the simplest omission, intensity-only imaging is necessarily blind to the phase of coherent light, an issue addressed by techniques such as phase contrast microscopy[1], which enables the direct visualization of transparent living microbes.

Moreover, as a transverse electromagnetic wave, light is vectorial in nature: light's polarization state, which is also absent in traditional intensity-only imaging, is classically defined as the direction of oscillation of the light's electric field vector. Polarization, as a design degree of freedom in optics and a source of additional information, has always been of interest and utility to both fundamental science and optical technologies[2,3]. The generation, manipulation, sensing and imaging of polarization is of importance because of the polarization's potential to reveal rich information about the physical properties of objects, materials and their structures, indiscernible to other optical techniques[4–6].

Polarization can be represented by a four-component vector known as a Stokes vector. A linear polarization-transforming interaction of light with an object that modifies the Stokes vector can be described fully by a 4 × 4 matrix, known as a Mueller matrix (MM). Polarization-transforming properties of an object, including its retardance, diattenuation, polarizance and depolarization, can all be directly computed from this MM[7]. MM imaging captures images of the spatially varying MM elements of a sample or object of interest, and provides one of the most complete descriptions of an object's optical properties, including its intensity response (given by the image of the first element M_{00}), its differential phase response (given by the retardance computed from a subset of Mueller elements) and its polarization response (defined by all 16 normalized Mueller components)—revealing information that would otherwise be invisible to traditional intensity-only imaging[8].

MM imaging has found important applications, most notably in biology and medicine[9,10]. Some examples include the use of MM imaging for disease diagnostics[11], retinal imaging[12], glucose sensing[13], bacteria detection[14], identification of malignant tissues[15], differentiation between healthy and cancerous tissues[16,17] (cancerous tissues, for

[1]Harvard John A. Paulson School of Engineering and Applied Sciences, Harvard University, Cambridge, MA, USA. [2]Department of Electrical and Computer Engineering, Jacobs School of Engineering, University of California San Diego, San Diego, CA, USA. [3]Institute of Nanotechnology, Karlsruhe Institute of Technology, Karlsruhe, Germany. ✉e-mail: zaidi01@g.harvard.edu; capassso@seas.harvard.edu

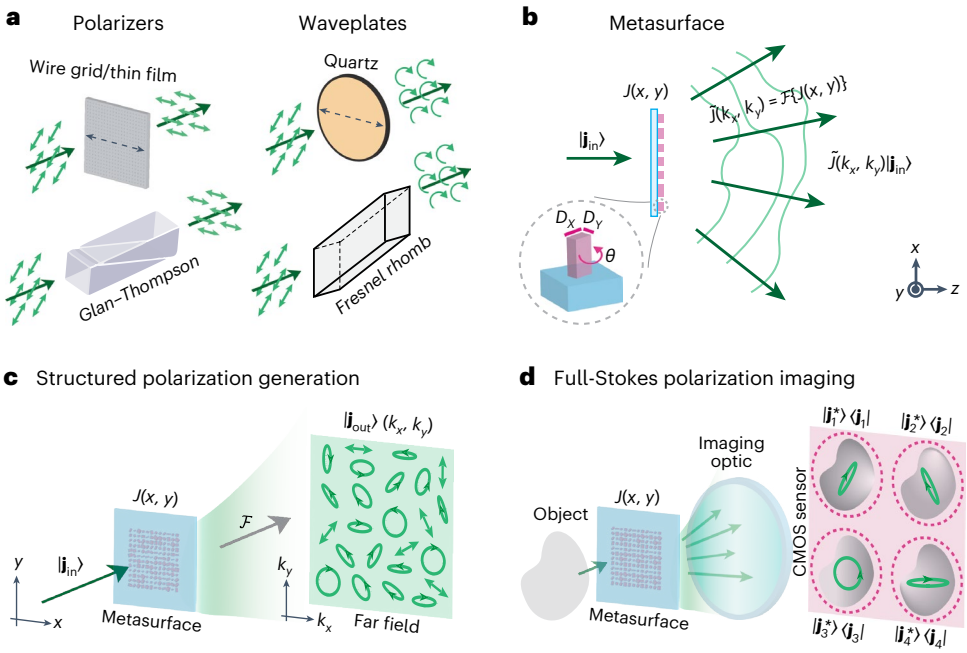

Fig. 1 | Conventional polarization optics versus metasurfaces. a, Examples of conventional polarization optics; owing to their bulk polarization response, they provide no spatial control over the resulting polarization. **b**, A metasurface—which can be described by a spatially varying Jones matrix distribution $J(x, y)$, and a far-field polarization response $\tilde{J}(k_x, k_y) = \mathcal{F}\{J(x, y)\}$, where $\mathcal{F}$ is the two-dimensional spatial Fourier transform—provides full spatial control over the resulting polarization. Each nanopillar provides three degrees of freedom—pillar length D_x, pillar width D_y and pillar orientation θ; the metasurface, composed of thousands of such nanopillars, has many degrees of freedom that can be optimized for the desired polarization response. **c**, A metasurface can be used for 'structured polarization' generation, where, for an incident polarization state $|\mathbf{j}_{in}\rangle$, the far-field output $|\mathbf{j}_{out}\rangle(k_x, k_y)$, given by $\tilde{J}(k_x, k_y)\,|\mathbf{j}_{in}\rangle$, follows a user-specified polarization distribution. **d**, A metasurface can also be designed to function as a polarization analyser with a Jones matrix response $\tilde{J} = |\mathbf{j}^*(k_x, k_y)\rangle\langle\mathbf{j}(k_x, k_y)|$, in the far field. A (periodic) metasurface—which splits the incoming light into its first four diffraction orders, and simultaneously analyses for four different polarization states—alongside an imaging lens and a sensor, can perform full-Stokes imaging.

instance, show different depolarization and retardance signatures compared with healthy tissues), and discerning between different types and stages of cancers[18]. The use of MM imaging has also been explored in areas such as ellipsometry[19], ocean science[20], turbidity[21] and target detection[6,8]. Despite the obvious advantages and utility of MM imaging, its widespread adoption has been hampered by the relative complexity, bulk, cost and hardware limitations of its existing implementations. In particular, because of many practical challenges, a single-shot MM imaging system has never been experimentally demonstrated. In our work, using metasurface optics, we propose and implement a compact, single-shot and complete MM imaging system that overcomes the limitations of existing MM imaging solutions, and the simplicity it provides may aid the widespread adoption of MM imaging.

Conventional versus metasurface polarization optics

Conventionally, polarization optics—such as wire-grid/thin-film polarizers, polarizating beamsplitters and crystalline waveplates, among others—transform the incident polarization owing to the bulk polarization response of their constituent elements. These components, while popular, allow only a limited set of polarization transformations, and provide no spatial control over the output polarization (Fig. 1a). A variety of relatively recent technologies, such as micro-patterning[22] and liquid crystals[23], do provide spatial polarization control, but present their own limitations: micro-patterning is usually limited to linear-only polarization transformations, and has poor spatial resolution[24]; liquid crystals often require multiple passes to address different states of polarization, needing space and introducing complexity[25]. As a result, MM imaging implementations relying on these components suffer from hardware limitations. For instance, the most popular MM imaging implementation uses the 'division of time' approach, where the sample is sequentially illuminated with and analysed for different polarization states, to compute the entire MM[26]. This approach, because of its finite time resolution, is infeasible for real-time imaging applications. Such an implementation also requires the use of multiple components and often uses moving parts, adding to the bulk, cost and complexity of the system. To mitigate these challenges, in particular the problem of time resolution, researchers have explored partial MM imaging implementations (where only a subset of the MM elements are measured)[27,28], hybrid implementations (consisting a mix of spatial and temporal control)[29,30] and non-imaging implementations[31–34], but a truly single-shot and complete MM imaging implementation has remained elusive. A handful of theoretical and conceptual frameworks that have been proposed for single-shot MM imaging—based on conventional polarization gratings[35], Savart plates[36] and division-of-focal-plane imaging[37]—all face unique practical challenges. For instance, the proposal to use conventional polarization gratings[35] or Savart plates[36] would severely limit the spatial resolution available because of channel redundancy and cross-talk, with such systems also requiring multiple polarization components (such as eight polarization gratings[35] or four Savart plates[36] on top of conventional polarizers and waveplates). Meanwhile division-of-focal-plane imaging sensors are challenging to fabricate for arbitrary polarizer designs[37]; commercially available division-of-focal-plane sensors as manufactured by, for example, SONY, are generally sensitive to only the linear polarization of light, and must be augmented to sense its ellipticity. Therefore, no convincing implementation for single-shot and complete MM imaging has been proposed so far.

Unlike more conventional polarization optics, metasurfaces[38,39]—subwavelength-spaced arrays of phase-shifting nanopillars—provide complete spatial control over polarization transformations, and allow us to most optimally sample the polarization space in both illumination

and analysis. A metasurface can be mathematically described as a spatially varying Jones matrix of the form

$$J(x,y) = R\left(-\theta(x,y)\right)\begin{pmatrix} e^{i\phi_X(x,y)} & 0 \\ 0 & e^{i\phi_Y(x,y)} \end{pmatrix} R\left(\theta(x,y)\right) \quad (1)$$

where (x, y) are spatial coordinates, and $R(\theta)$ is the 2×2 rotation matrix[40,41]. The three degrees of freedom at each (x, y), $\theta(x, y)$, $\phi_X(x, y)$ and $\phi_Y(x, y)$, are directly related to the shape, including the length (D_X), width (D_Y), orientation (θ) and height (kept constant) of the local nanopillar (Fig. 1b), showing strong structural birefringence[40,41]. As seen in equation (1), a metasurface locally performs unitary transformations only, but through interference, its far-field response can be both unitary (waveplate-like) and/or Hermitian (polarizer-like)[42,43]. Engineering the far field to perform user-specified polarization transformations is of great utility because of the far field's ease of access, for instance, by choosing a suitable operating distance or using a lens. For a metasurface with a spatially varying Jones matrix $J(x, y)$, the polarization response in the far field (Fig. 1b) can be most succinctly described as $\tilde{J}(k_x, k_y) = \mathcal{F}\{J(x,y)\}$, using matrix Fourier optics[44], where $\mathcal{F}$ is the two-dimensional spatial Fourier transform operator. We can then optimize a metasurface profile $J(x, y)$, using algorithms such as gradient descent or phase retrieval[45], to perform any conceivable polarization transformations $\tilde{J}(k_x, k_y)$in the far field. A metasurface can be designed to, as shown in Fig. 1c, generate user-specified spatially varying states of polarization for a given incident polarization[43,46,47], or as shown in Fig. 1d, analyse for different polarization states in separate diffraction orders for full-Stokes imaging[44,48]. Owing to their versatility, metasurfaces provide an ideal platform for compact, single-shot and complete MM imaging.

Theory and design of single-shot and complete MM imaging

Traditionally speaking, a photograph or an image of a non-luminous object describes the spatially varying intensity distribution of transmitted or reflected light under some external illumination. Full-Stokes imaging, of the type shown in Fig. 1d, can describe both the intensity and polarization distribution of light over the entire field of view—but the resulting 'polarization image' is still incomplete in describing the polarization properties of an object of interest. An object may transmit or reflect a certain distribution of intensity and polarization, given an incident polarization (distribution); however, it might produce a completely different intensity and polarization response under a different set of incident polarizations (Fig. 2a). A complete 'polarization image' is thus an image that can describe the response of an object to not only a given incident polarization but also all possible incident polarizations—a 4×4 MM image (Fig. 2b). An object that may appear invisible or ordinary under standard intensity-only imaging may in fact show rich contrast and distinct features in its MM image.

For a truly single-shot and complete MM imaging system, the information to compute all 16 images that make up a MM image would need to be acquired in a single measurement in time. To do this, we illuminate the object with a polarization distribution described by the following spatially varying Stokes vector

$$\mathbf{S}_{\text{in}}(m,n) = \begin{pmatrix} 1 \\ \sqrt{2/3}\cos(0.5m\pi)\cos(n\pi) \\ \sqrt{2/3}\sin(0.5m\pi)\cos(n\pi) \\ \sqrt{1/3}\cos(m\pi) \end{pmatrix} \quad (2)$$

where m and n are discrete spatial (pixel) coordinates. (Because of the use of digital electronics in both computation and measurement, it is best to describe the formulation in terms of discrete spatial coordinates.) For each discrete value of m and n, equation (2) describes a physical state of polarization. In total, the polarization distribution defined by equation (2) consists of four unique polarization states (which make up the vertices of a tetrahedron inscribed within the Poincare sphere) arranged in a 2×4 repeating unit cell (Fig. 2c). This particular structured polarization illumination (equation (2)) is chosen to most optimally sample the polarization space (Supplementary Section 1). From equation (2), we see that the individual Stokes components of the structured polarization illumination are sinusoids in the spatial domain, and delta functions in the Fourier domain or momentum (k) space (Fig. 2d). Let us now consider an object whose polarization properties are described by its spatially varying MM

$$\hat{M}_{\text{obj}}(m,n) = \begin{pmatrix} M_{00}(m,n) & M_{01}(m,n) & M_{02}(m,n) & M_{03}(m,n) \\ M_{10}(m,n) & M_{11}(m,n) & M_{12}(m,n) & M_{13}(m,n) \\ M_{20}(m,n) & M_{21}(m,n) & M_{22}(m,n) & M_{23}(m,n) \\ M_{30}(m,n) & M_{31}(m,n) & M_{32}(m,n) & M_{33}(m,n) \end{pmatrix} \quad (3)$$

When the structured polarization illumination (equation (2)) interacts with the object (equation (3)), the resulting output Stokes vector can be described as

$$\mathbf{S}_{\text{out}}(m,n) = \begin{pmatrix} M_{00} + M_{01}\sqrt{2/3}\cos(0.5m\pi)\cos(n\pi) + M_{02}\sqrt{2/3}\sin(0.5m\pi)\cos(n\pi) + M_{03}\sqrt{1/3}\cos(m\pi) \\ M_{10} + M_{11}\sqrt{2/3}\cos(0.5m\pi)\cos(n\pi) + M_{12}\sqrt{2/3}\sin(0.5m\pi)\cos(n\pi) + M_{13}\sqrt{1/3}\cos(m\pi) \\ M_{20} + M_{21}\sqrt{2/3}\cos(0.5m\pi)\cos(n\pi) + M_{22}\sqrt{2/3}\sin(0.5m\pi)\cos(n\pi) + M_{23}\sqrt{1/3}\cos(m\pi) \\ M_{30} + M_{31}\sqrt{2/3}\cos(0.5m\pi)\cos(n\pi) + M_{32}\sqrt{2/3}\sin(0.5m\pi)\cos(n\pi) + M_{33}\sqrt{1/3}\cos(m\pi) \end{pmatrix} \quad (4)$$

where we omit the (m, n) dependence of the Mueller components for brevity. From equation (4), we see that the amplitudes of the different spatial carrier waves given by the Stokes elements defined in equation (2) are modulated independently by the different MM components. This amplitude modulation can be best understood in k-space, by studying the Fourier spectra $\tilde{\mathbf{S}}_{\text{out}}(\mu, \eta)$—where (μ, η) are the k-space coordinates, analogues to spatial coordinates (m, n)—of the output Stokes vector, defined in terms of convolutions involving the Fourier spectra of the MM components, and the incident Stokes elements. As seen in Fig. 2e, the spectra of every MM component is shifted (by the Fourier shift theorem) to separate locations or 'channels' in the k-space, where these channels are centred on the delta functions given by the (spatial) spectra of the incident Stokes elements. To avoid any overlap between neighbouring spectra of the MM components (aliasing), the separation between two neighbouring channels needs to be at least twice the maximum spatial frequency of the spectra of the MM components centred on those channels (Nyquist theorem). If the spectra of each MM component is indeed band-limited and within the Nyquist limit, the image of each MM component can be retrieved without any loss of information. This can be accomplished by the amplitude

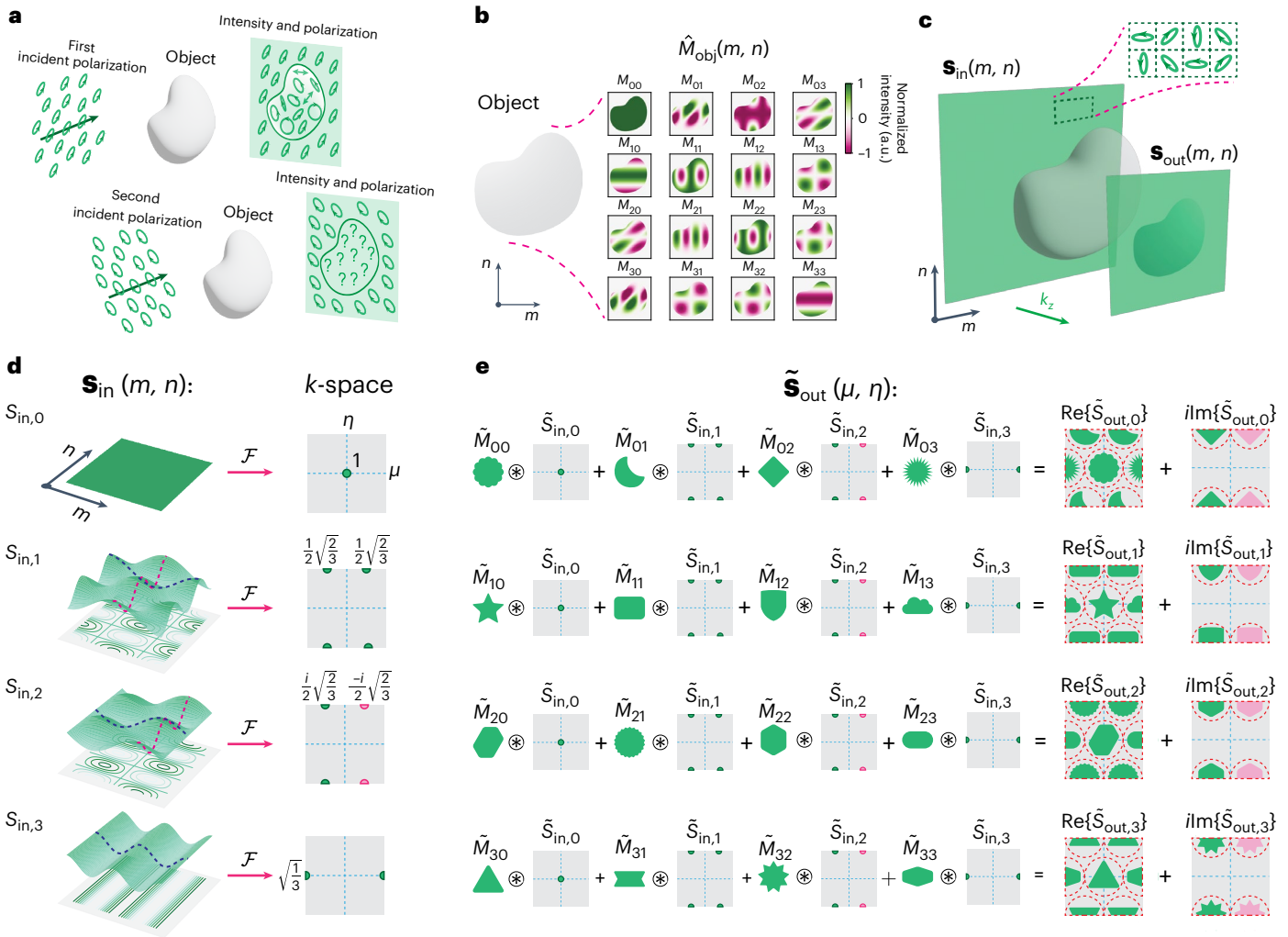

Fig. 2 | Concept of single-shot and complete MM imaging. a, For a given incident polarization, an object, in general, produces a spatially varying intensity and polarization response in transmission or reflection. For a different incident polarization, the object may produce a completely different response. **b**, To quantify this response, we have to calculate a set of 16 images that correspond to its 4 × 4 MM image. An object's MM image can reveal rich contrast, making it much easier to classify. **c**, We can spatially sample the object with a minimum of four different incident polarization states $\mathbf{S}_{in}(m, n)$, where the resulting polarization distribution $\mathbf{S}_{out}(m, n) = \hat{M}_{obj}(m, n)\mathbf{S}_{in}(m, n)$ can be imaged by a full-Stokes camera. **d**, The different Stokes components of the incident polarization states are spatially varying and orthogonal sinusoids with different spatial frequencies and thus non-overlapping delta functions in the Fourier domain. **e**, $\mathbf{S}_{out}(m, n) = \hat{M}_{obj}(m, n)\mathbf{S}_{in}(m, n)$, instead of multiplications, can be described in terms of convolutions (⊛) in the Fourier domain. We see that the Fourier spectra of the different components of the object's MM, $\hat{M}_{obj}(m, n)$, 'shift' to the location of the different delta functions. If the spectra of the Mueller components are sufficiently band-limited, they can be 'filtered' from the resulting Stokes image, allowing the full reconstruction of $\hat{M}_{obj}(m, n)$.

demodulation of the signal(s) in $\mathbf{S}_{out}$ (equation (4)). Thus, if $\mathbf{S}_{out}$ can be acquired in a single measurement, all the MM components can also be computed in a single measurement—resulting in a truly single-shot and complete MM imaging system.

Experimental implementation using metasurfaces

There are two key modules in our single-shot and complete MM imaging system: structured polarization illumination (using 'metasurface 1'), and full-Stokes imaging (using 'metasurface 2'). Metasurface 1 generates $\mathbf{S}_{in}(m, n)$ (equation (2)) and metasurface 2 analyses $\mathbf{S}_{out}(m, n)$ (equation (4)) in a single shot, from which the MM image, $\hat{M}_{obj}(m, n)$ (equation (3)), is computed using the principles defined above. Metasurface 1 and metasurface 2, having separate functions, are computationally optimized using different algorithms; however, they are fabricated using the exact same method[49] (Methods). The fabricated metasurfaces are composed of TiO_2 nanopillars, designed to work with our wavelength of choice (green, 532 nm) in the visible spectrum, with efficiencies similar to past reported works[42–44]. (It should be noted that the design principles in our work are wavelength agnostic.) Metasurface 1 is composed of an aperiodic arrangement of roughly 4,000 nanopillars, with each pillar separated by a subwavelength distance of 420 nm, yielding a metasurface roughly 1.68 mm in diameter. The structured polarization illumination or 'hologram' (with a divergence angle θ_{div} of ±40°) diverges quickly, and it is best, in practice, to use a converging lens to access its far field. Metasurface 2 consists of a periodic arrangement of 12 × 12 arrays of nanopillars (again, separated by 420 nm) and is approximately 3 mm in diameter. Metasurface 2, with a larger diameter size, allows for more light to pass through the aperture for imaging.

In our proof-of-concept implementation (Fig. 3a), we use a 4*f* imaging system to give us control over the spatial and angular (de) magnification of the fields, to completely image the object onto the spatial extent of the complementary metal–oxide–semiconductor (CMOS) sensor, but its use is not fundamental to our design. The sizes and dimensions of the metasurfaces, CMOS sensor, the imaging optic and the distances between them can be chosen to eliminate the need

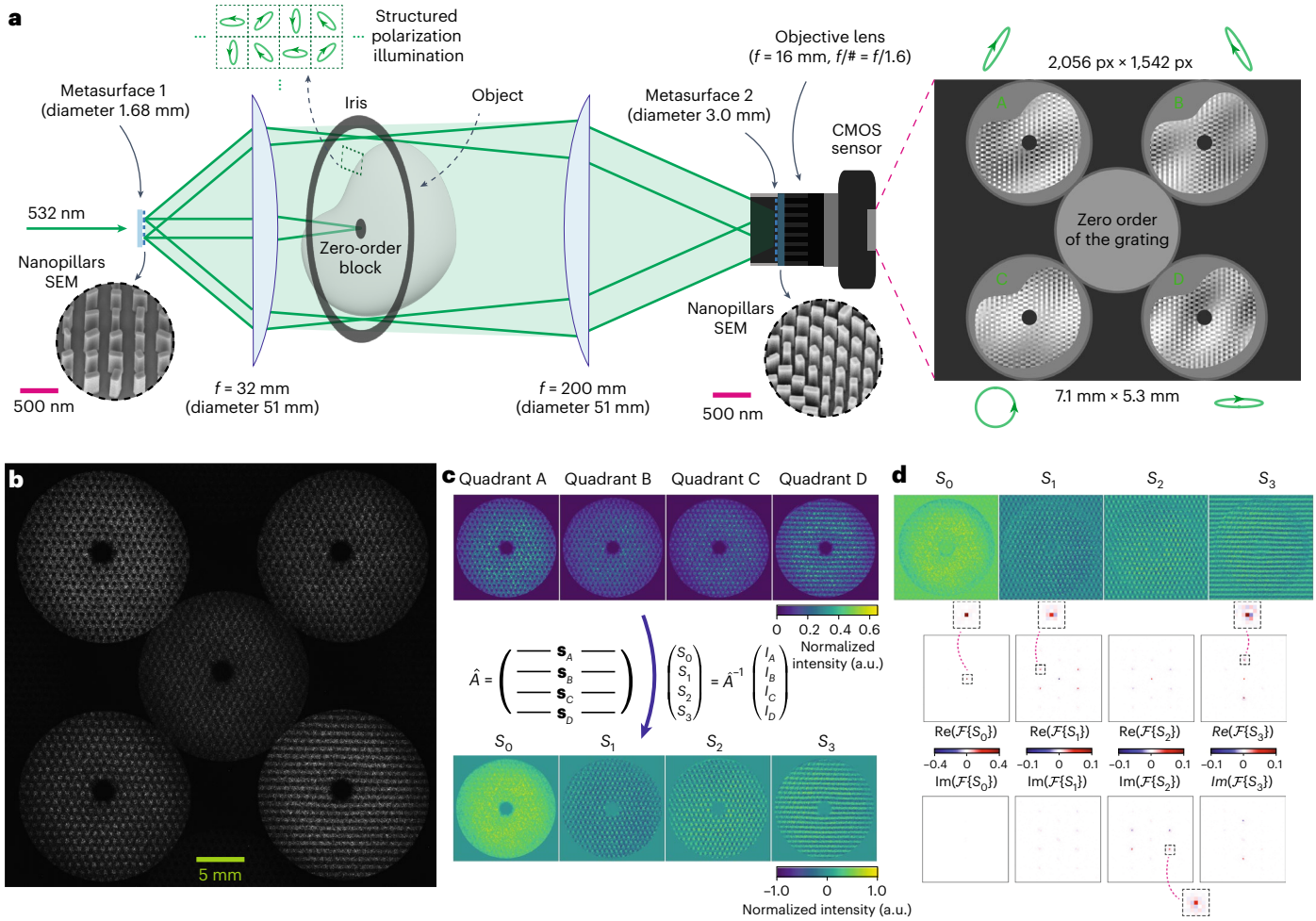

Fig. 3 | Experimental implementation. a, A 4*f* imaging system is used to image the MM of the object, which is placed in the 'Fourier plane', conjugate to both metasurfaces. Metasurface 1 produces structured polarized light which illuminates the object, and metasurface 2 diffracts and analyses the resulting fields that are imaged onto the CMOS sensor. The iris in the Fourier domain is placed to limit the FOV, and the zero-order block is placed to prevent the zeroth order from saturating the sensor. **b**, Raw image produced by the system without any object, revealing the periodically structured polarization. This image of 'air' (identity MM) can be used for calibration. Using the scale bar, one can estimate that the 'pixel' resolution—the area that belongs to a given state of structured polarization—is 0.5 mm. **c**, The raw images in the four quadrants of the CMOS sensor can be converted to a full-Stokes image by using the instrument matrix, which is predetermined in a separate calibration. **d**, The region with no signal can be 'filled' via extrapolation—resulting in images or signals that are close to two-dimensional sinusoids. These images are used as reference images for amplitude demodulation. The Fourier spectra of these reference images are close to the expected delta-like functions.

of a 4*f* system, depending on the application (a miniaturized, fieldable version of the system could consist of just a laser illumination source, a metasurface to create structured polarization illumination and a metasurface polarization imager). The lenses in the 4*f* system can also be replaced by metalenses[50], for a truly flat optic implementation. The object is placed in the 'Fourier plane', conjugate to both metasurface 1 and metasurface 2. An iris and a zero-order beam block (circular black Acktar tape on a glass substrate) are also placed in the Fourier plane to limit the field of view (FOV) and block the background zeroth-order light, respectively. The object, now in the far field of metasurface 1, interacts with the structured polarization illumination; the resulting fields, in transmission and/or in reflection, are then imaged by the full-Stokes camera to retrieve the complete MM image.

The reconstruction accuracy of the MM image is directly related to the accuracy of the full-Stokes camera. It is important, thus, to independently design and calibrate a robust metasurface full-Stokes camera, as we have previously demonstrated[44,48,51], before introducing it into the MM imaging set-up. Our metasurface full-Stokes camera consists of metasurface 2, an imaging optic and a CMOS sensor. Metasurface 2 functions as both a diffraction grating (to 'split amplitudes') and an analyser to simultaneously analyse for polarization states in different diffraction orders. In particular, metasurface 2 analyses for four different polarization states (which, again, make up the vertices of a tetrahedron inscribed within the Poincare sphere), in the first four off-axis diffraction orders. When a scene, extended over some FOV, is incident on metasurface 2, the separately analysed copies of the scene in the four diffraction orders can be imaged onto a CMOS sensor using an imaging optic. The four-element Stokes vector necessitates at least four measurements to be fully determined (at each pixel), hence the use of four diffraction orders (and not any less). If the metasurface grating is designed to analyse for the four polarization states $\mathbf{S}_A$, $\mathbf{S}_B$, $\mathbf{S}_C$ and $\mathbf{S}_D$ on its inner four diffraction orders, then given an incident spatially varying Stokes vector $\mathbf{S}_{out}$, the four-element 'intensity vector' (a vector of images) $\mathbf{I}_{out}(m, n)$ can be written as

$$\overbrace{\begin{pmatrix} I_{out,A}(m,n) \\ I_{out,B}(m,n) \\ I_{out,C}(m,n) \\ I_{out,D}(m,n) \end{pmatrix}}^{\mathbf{I}_{out}(m,n)} = \overbrace{\begin{pmatrix} \mathbf{S}_A \\ \mathbf{S}_B \\ \mathbf{S}_C \\ \mathbf{S}_D \end{pmatrix}}^{\hat{A}} \overbrace{\begin{pmatrix} S_{out,0}(m,n) \\ S_{out,1}(m,n) \\ S_{out,2}(m,n) \\ S_{out,3}(m,n) \end{pmatrix}}^{\mathbf{S}_{out}(m,n)} \quad (5)$$

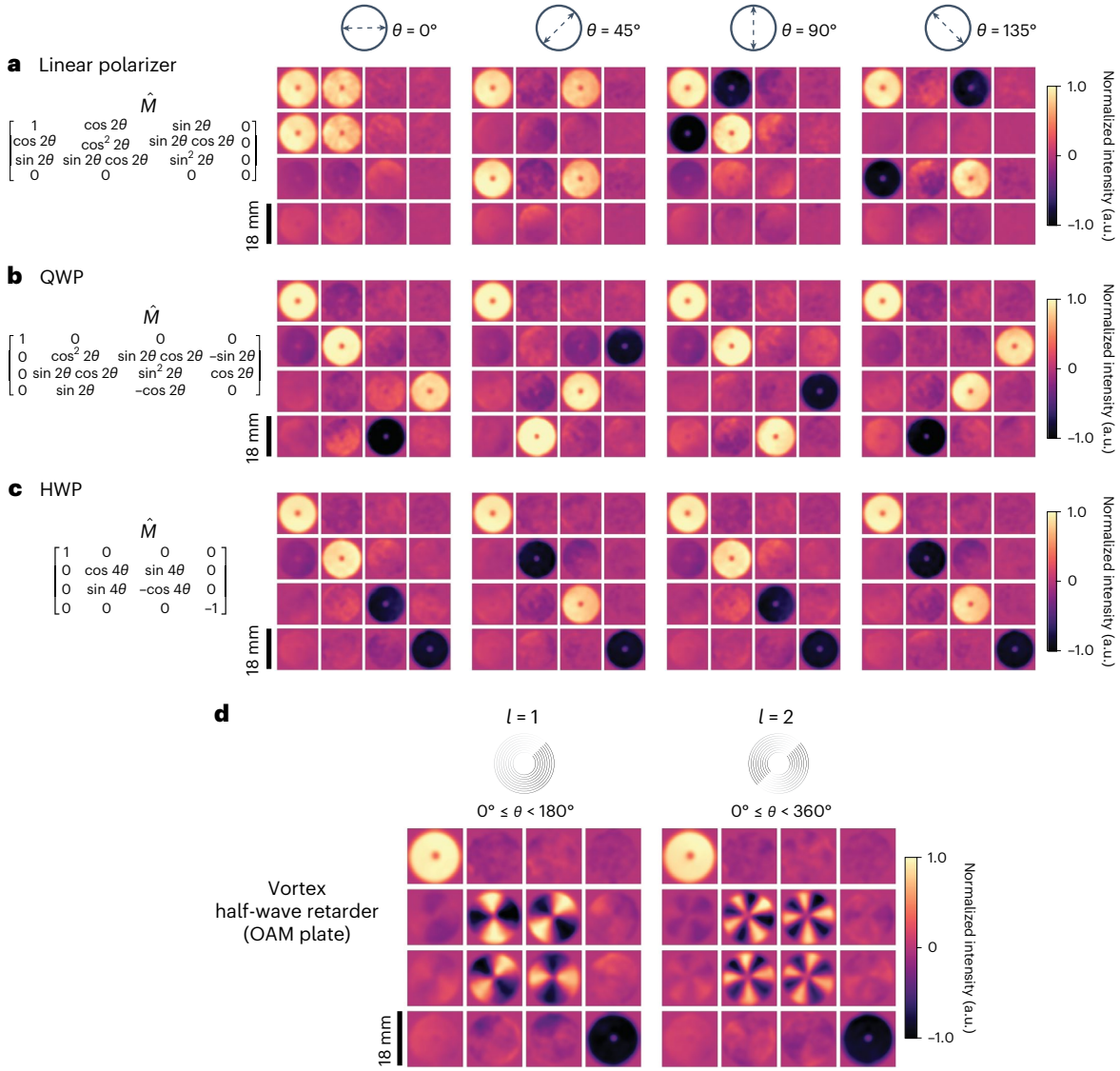

Fig. 4 | MM imaging results for transmission. a, Measured MM images of a thin-film linear polarizer at four different transmission-axis orientations (θ). Also listed is the MM ($\hat{M}$) of the linear polarizer as a function of θ. **b**, Measured MM images of a zero-order quartz QWP at four different fast-axis orientations (θ). Also listed is the MM ($\hat{M}$) of the QWP as a function of θ. **c**, Measured MM images of a zero-order quartz HWP at four different fast-axis orientations (θ). Also listed is the MM ($\hat{M}$) of the HWP as a function of θ. **d**, Measured MM images of two vortex half-wave retarders (OAM plates), for the two helical modes $l = 1$ and $l = 2$.

where $\hat{A}$ is referred to as the instrument matrix. Using equation (5), $\mathbf{S}_{out}$ can be determined—pixel by pixel at each (m, n) over the entire FOV—by using the inverse of the instrument matrix, $\hat{A}^{-1}$. The instrument matrix $\hat{A}$ is experimentally determined through a calibration[48,51], to calibrate out discrepancies between the ideal design and its practical implementation by metasurface 2.

Figure 3b shows the raw greyscale image output by the system in the case of no object (or simply 'air'). We can see the circular edges of the iris and the circular beam block. The iris, functioning as a field stop, limits the FOV and prevents the scenes centred on different diffraction orders from overlapping with each other. The zeroth-order beam block prevents the strong background laser light from propagating through the system and saturating the sensor. The raw image can be processed into a full-Stokes image using the instrument matrix $\hat{A}$ (Fig. 3c). We can then compute the complete MM image through amplitude demodulation of the full-Stokes image. There are different methods and algorithms to demodulate a signal from a carrier wave; here, we use the 'product detector' method. In this method, the amplitude-modulated signal is multiplied by the carrier wave, followed by a low-pass filter (Supplementary Section 3). This method requires the knowledge of the carrier wave, which necessitates a reference measurement. In our case, the 'air' image serves as the reference measurement, as air has a spatially uniform and identity MM. The reference measurement also helps us calibrate out any spatial variations in the overall intensity of our structured polarization illumination. To prepare the air Stokes image as a reference measurement to be used in demodulation, we complete parts of the image with no signal (corresponding to the regions where light is blocked from the iris and the beam block), through extrapolation (Fig. 3d). This ensures that the reference Stokes components are close to the desired sinusoid signals. This can be seen in the Fourier spectra of the reference Stokes components—we see (approximate) delta functions in the expected channel locations (Fig. 3d).

Transmission and reflection measurement results

We use our system to image a variety of commercially available polarization optics, such as polarizers, waveplates and orbital-angular-momentum (OAM) plates. The results are summarized in Fig. 4.

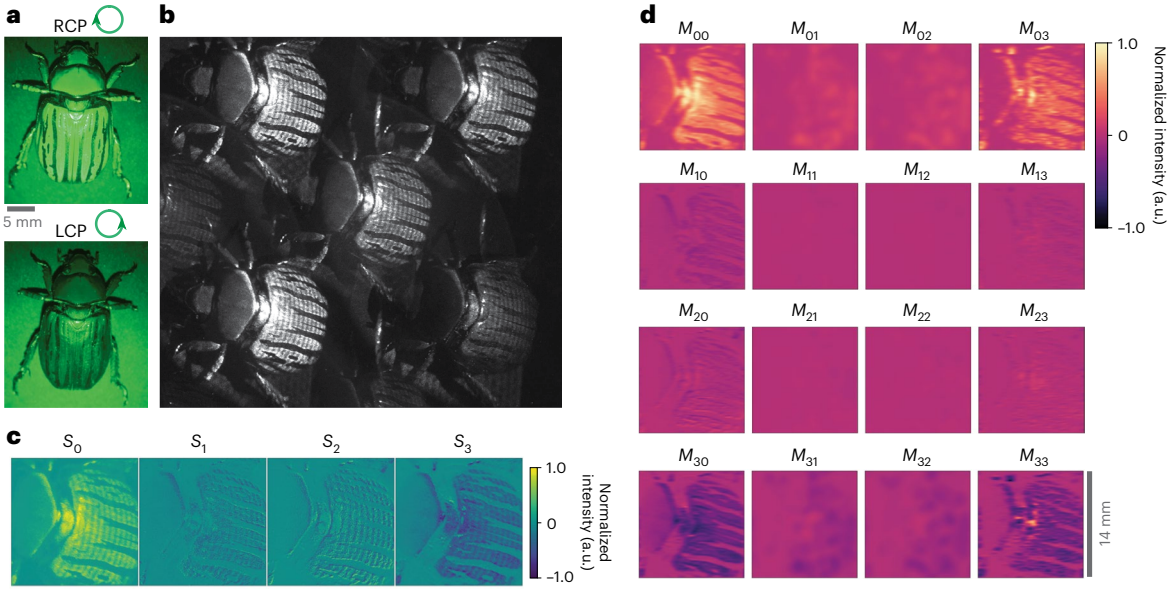

Fig. 5 | MM imaging results for reflection. a, *Chrysina gloriosa*, more commonly referred to as the 'chiral beetle', is illuminated by RCP light and LCP light, and imaged by a standard digital camera. The intensity images, juxtaposed for comparison, show that the beetle exhibits a different optical response for the two circular polarizations. **b**, Raw image of the chiral beetle captured using our MM imaging system. **c**, The resulting full-Stokes image computed from the raw image, using the instrument matrix $\hat{A}$ (equation (5)). **d**, The resulting MM image from the full-Stokes image, is computed (demodulated and normalized) using a reference-free method (Supplementary Section 3). The MM image of the chiral beetle has spatially resolved features such as the size and shape of the shell, and the characteristic striae (or lines) on the shell; it also confirms that the shell of the chiral beetle functions as a homogeneous circular polarizer.

We image a linear film polarizer (Fig. 4a), a zero-order quarter-waveplate (QWP; Fig. 4b) and a zero-order half-waveplate (HWP; Fig. 4c), each in four different orientations, resulting in 12 different MM images. The expected (theoretical) MM responses of these optics as a function of different orientations (θ) are also listed in Fig. 4a–c. We see good correspondence between the measured MM images and the expected responses. Furthermore, we can easily identify the regions where the light is blocked by the iris and the beam block, having MM values of zero. The edges of the iris and the circular beam block, in a way, provide us with additional spatial information to image and test our system beyond just the 'polarization active' region of the optics. A MM is often normalized with respect to its M_{00} component. For an MM image, normalizing each pixel with respect to its M_{00} component will result in the loss of the overall (polarization insensitive) intensity variation across the image. Therefore, we normalize each pixel of all the components of the MM image by the maximum pixel value of the M_{00} image. (Following normalization, saturated pixels, with non-physical values beyond ±1, are clipped at ±1. Saturated pixels, still, have values very close to ±1, as seen in our analysis in Supplementary Fig. 10.) We also image two OAM plates, the results of which are shown in Fig. 4d. In particular, these are vortex half-wave retarders made of liquid crystal polymers, with a fixed retardance of π, but a fast-axis that rotates azimuthally over the area of the optic (that is, a geometric phase device). This spatial variation is unambiguously captured in the M_{11}, M_{12}, M_{21} and M_{22} components in the two Mueller images shown in Fig. 4d.

As explained above, we calibrate the full-Stokes camera and perform reference measurements for the structured polarization illumination—still, inevitably, there remain sources of error that can degrade the quality of the final image. Contributions from high-spatial-frequency components from, for instance, the sharp edges of the iris and the beam block, can result in aliasing, although empirically, we find these contributions to be negligible (Supplementary Section 1). A main source of error is the channel 'cross-talk'. The Stokes components defined in equation (2) are ideally all orthogonal to each other, but in practice, when implemented by the metasurface, the resulting reference Stokes components (Fig. 3d) are not completely orthogonal, resulting in (small) mixing of the spectra of different Mueller components, or cross-talk.

We also test our system for imaging in reflection. We decided to image *Chrysina gloriosa*, or the 'chiral beetle', which is known to have different optical responses for the two circular polarizations. As shown in Fig. 5a, parts of the exoskeleton or shell of the chiral beetle appear bright under right-circular polarization (RCP) illumination and dark under left-circular polarization (LCP) illumination (for the green wavelength). Thus, we can ascertain that the shell of the chiral beetle is analysing for circular polarization; still, we cannot conclude the state of polarization reflecting off of the shell from these two intensity measurements. Our MM imaging system, set up in reflection, allows us to determine the exact polarization properties of the shell of the chiral beetle (Fig. 5b–d). We could not determine a suitable reflective object for reference Stokes measurements in reflection, due to the curvature of the beetle's shell as evident in the raw image (Fig. 5b). Therefore, to compute the MM image (Fig. 5d) from the Stokes image (Fig. 5c), we use a reference-free method, by using contextual knowledge and some simplifying assumptions (Supplementary Section 3). From the resulting MM image of the chiral beetle (Fig. 5d), we can determine that its shell behaves as a homogeneous circular polarizer—it not only analyses for circular polarization but also generates circular polarization in reflection. Interesting spatial features such as the striae (characteristic dark lines on the shell of the chiral beetle) are also resolved in the final MM image (Fig. 5d), by using a rectangular low-pass filter, assigning more bandwidth along one axis compared with the other (Supplementary Section 3).

Discussion and conclusion

In our work, we have described the principles behind designing and building a compact, single-shot and complete MM imaging system, and using these principles, implemented the described system to successfully image objects in both transmission and reflection. In designing our system, we settled on a resolution that was sufficient for our

proof-of-concept measurements. By designing larger metasurfaces, using higher-numerical-aperture lenses and higher-resolution sensors, the resolution of the MM imaging system can be improved to enable different applications (Supplementary Section 4). More sophisticated calibration methods and reconstruction algorithms, for instance, by custom-designing the Fourier filters[52], can be used to further reduce errors from aliasing and cross-talk. Existing super-resolution techniques and machine learning-assisted reconstruction can also be used to image beyond the band limits of the filters[53]. Furthermore, the structured polarization illumination can be used to probe the depth profile of the object in addition to its polarization properties, for polarization-resolved depth sensing. (For example, the curvature of the lines reflecting off of the shell of the chiral beetle in Fig. 5b could be potentially used to estimate its curvature). These directions will be the subject of future work.

The MM imaging system we present illustrates the ability of metasurfaces to greatly simplify the design and architecture of devices and systems based on polarization optics. Our work should be of greatest practical utility in applications requiring both compact and single-shot polarization imaging. Important examples of such applications in biomedicine include the imaging of live tissue samples in microscopy[54], polarimetric endoscopic imaging[55,56], retinal scanning[12] and non-/minimally invasive imaging of cancerous tumours[10]. Advanced optical sensing in consumer electronics, such as facial recognition in smartphones, and eye-tracking in augmented and virtual reality headsets, should also greatly benefit from the small form factor of our system for complete and single-shot MM imaging. The potential of single-shot MM imaging in saccharimetry (the process of measuring the amount of sugar in a sample) should be useful to food, pharmaceutical and biomedical industries[13]. Compact and single-shot MM imaging, fittingly, could also be of great use in the characterization of nanostructures, metasurfaces and metamaterials[57,58]. Furthermore, our system, given its superior time resolution and flexibility, could be useful in generating large MM datasets to train neural networks for many machine learning classification applications. Beyond technological applications, our work could be of consequence in fundamental science, such as in the detection of the time-varying birefringence of vacuum in the presence of intense electric and magnetic fields (as theorized by quantum electrodynamics)[59], in the study of three-dimensional polarization states of light[60], and in research on both short-wavelength (X-ray)[61] and long-wavelength (terahertz) polarimetry[62]. This should inspire research in exciting new directions.

References

1. Zernike, F. How I discovered phase contrast. *Science* **121**, 345–349 (1955).
2. Snik, F. et al. An overview of polarimetric sensing techniques and technology with applications to different research fields. *Proc. SPIE* **9099**, 90990B (2014).
3. Damask, J. N. *Polarization Optics in Telecommunications* (Springer, 2005).
4. Tyo, J. S., Goldstein, D. L., Chenault, D. B. & Shaw, J. A. Review of passive imaging polarimetry for remote sensing applications. *Appl. Opt.* **45**, 5453–5469 (2006).
5. Demos, S. G. & Alfano, R. R. Optical polarization imaging. *Appl. Opt.* **36**, 150–155 (1997).
6. Tyo, J. S., Rowe, M. P., Pugh, E. N. & Engheta, N. Target detection in optically scattering media by polarization-difference imaging. *Appl. Opt.* **35**, 1855–1870 (1996).
7. Lu, S.-Y. & Chipman, R. A. Interpretation of Mueller matrices based on polar decomposition. *J. Opt. Soc. Am. A* **13**, 1106–1113 (1996).
8. Azzam, R. M. A. Stokes-vector and Mueller-matrix polarimetry [invited]. *J. Opt. Soc. Am. A* **33**, 1396–1408 (2016).
9. Tuchin, V. V., Wang, L. V. & Zimnyakov, D. A. *Optical Polarization in Biomedical Applications* (Springer, 2006).
10. Alali, S. & Vitkin, A. Polarized light imaging in biomedicine: emerging Mueller matrix methodologies for bulk tissue assessment. *J. Biomed. Opt.* **20**, 061104 (2015).
11. Dubreuil, M. et al. Mueller matrix polarimetry for improved liver fibrosis diagnosis. *Opt. Lett.* **37**, 1061–1063 (2012).
12. Dreher, A. W., Reiter, K. & Weinreb, R. N. Spatially resolved birefringence of the retinal nerve fiber layer assessed with a retinal laser ellipsometer. *Appl. Opt.* **31**, 3730–3735 (1992).
13. Westphal, P., Kaltenbach, J.-M. & Wicker, K. Corneal birefringence measured by spectrally resolved Mueller matrix ellipsometry and implications for non-invasive glucose monitoring. *Biomed. Opt. Express* **7**, 1160–1174 (2016).
14. Li, X. et al. Classification of morphologically similar algae and cyanobacteria using Mueller matrix imaging and convolutional neural networks. *Appl. Opt.* **56**, 6520–6530 (2017).
15. Ghosh, N. & Vitkin, I. A. Tissue polarimetry: concepts, challenges, applications, and outlook. *J. Biomed. Opt.* **16**, 110801 (2011).
16. Antonelli, M.-R. et al. Mueller matrix imaging of human colon tissue for cancer diagnostics: how Monte Carlo modeling can help in the interpretation of experimental data. *Opt. Express* **18**, 10200–10208 (2010).
17. Pierangelo, A. et al. Polarimetric imaging of uterine cervix: a case study. *Opt. Express* **21**, 14120–14130 (2013).
18. Novikova, T., Pierangelo, A., Martino, A. D., Benali, A. & Validire, P. Polarimetric imaging for cancer diagnosis and staging. *Opt. Photon. News* **23**, 26–33 (2012).
19. Liu, S., Chen, X. & Zhang, C. Development of a broadband Mueller matrix ellipsometer as a powerful tool for nanostructure metrology. *Thin Solid Films* **584**, 176–185 (2015).
20. Kokhanovsky, A. A. Parameterization of the Mueller matrix of oceanic waters. *J. Geophys. Res.* https://doi.org/10.1029/2001jc001222 (2003).
21. Kattawar, G. W. & Gray, D. J. Mueller matrix imaging of targets in turbid media: effect of the volume scattering function. *Appl. Opt.* **42**, 7225–7230 (2003).
22. Andreou, A. & Kalaylian, Z. Polarization imaging: principles and integrated polarimeters. *IEEE Sens. J.* **2**, 566–576 (2002).
23. Andrienko, D. Introduction to liquid crystals. *J. Mol. Liq.* **267**, 520–541 (2018).
24. Ratliff, B. M., LaCasse, C. F. & Tyo, J. S. Interpolation strategies for reducing IFOV artifacts in microgrid polarimeter imagery. *Opt. Express* **17**, 9112–9125 (2009).
25. Davis, J. A. et al. Diffraction gratings generating orders with selective states of polarization. *Opt. Express* **24**, 907–917 (2016).
26. Berezhnyy, I. & Dogariu, A. Time-resolved Mueller matrix imaging polarimetry. *Opt. Express* **12**, 4635–4649 (2004).
27. Gonzalez, M. et al. Design and implementation of a portable colposcope Mueller matrix polarimeter. *J. Biomed. Opt.* https://doi.org/10.1117/1.jbo.25.11.116006 (2020).
28. Tyo, J. S., Rodríguez-Herrera, O. G., Flannery, C., Kurtz, J. & Alenin, A. S. Scene-adaptive spatially channeled imaging Mueller polarimeter. *Opt. Express* **31**, 23678–23692 (2023).
29. Angelo, J. P., Germer, T. A. & Litorja, M. Structured illumination Mueller matrix imaging. Biomed. *Opt. Express* **10**, 2861–2868 (2019).
30. Huang, T. et al. Fast Mueller matrix microscope based on dual DoFP polarimeters. *Opt. Lett.* **46**, 1676–1679 (2021).
31. Gao, C. et al. Dual vortex retarder Mueller matrix ellipsometry. *Opt. Lasers Eng.* **166**, 107564 (2023).

32. Bhattacharyya, K. & Otani, Y. Single shot Mueller matrix polarimetry using axially symmetric quarter wave plate and channeled spectrum. *Optik* **183**, 451–454 (2019).
33. Töppel, F., Aiello, A., Marquardt, C., Giacobino, E. & Leuchs, G. Classical entanglement in polarization metrology. *New J. Phys.* **16**, 073019 (2014).
34. Pierangeli, D. & Conti, C. Single-shot polarimetry of vector beams by supervised learning. *Nat. Commun.* **14**, 1831 (2023).
35. Kudenov, M. W., Escuti, M. J., Hagen, N., Dereniak, E. L. & Oka, K. Snapshot imaging Mueller matrix polarimeter using polarization gratings. *Opt. Lett.* **37**, 1367–1369 (2012).
36. Cao, Q. et al. Snapshot imaging Mueller matrix polarimeter using modified savart polariscopes. *Appl. Opt.* **62**, 2124–2129 (2023).
37. Zaidi, A., McEldowney, S., Lee, Y.-H., Chao, Q. & Lu, L. Towards compact and snapshot channeled Mueller matrix imaging. *Opt. Lett.* **47**, 722–725 (2022).
38. Yu, N. et al. Light propagation with phase discontinuities: generalized laws of reflection and refraction. *Science* **334**, 333–337 (2011).
39. Yu, N. & Capasso, F. Flat optics with designer metasurfaces. *Nat. Mater.* **13**, 139–150 (2014).
40. Arbabi, A., Horie, Y., Bagheri, M. & Faraon, A. Dielectric metasurfaces for complete control of phase and polarization with subwavelength spatial resolution and high transmission. *Nat. Nanotechnol.* **10**, 937–943 (2015).
41. Mueller, J. B., Rubin, N. A., Devlin, R. C., Groever, B. & Capasso, F. Metasurface polarization optics: independent phase control of arbitrary orthogonal states of polarization. *Phys. Rev. Lett.* https://doi.org/10.1103/physrevlett.118.113901 (2017).
42. Zaidi, A., Rubin, N. A., Dorrah, A. H., Park, J.-S. & Capasso, F. Generalized polarization transformations with metasurfaces. *Opt. Express* **29**, 39065–39078 (2021).
43. Rubin, N. A., Zaidi, A., Dorrah, A. H., Shi, Z. & Capasso, F. Jones matrix holography with metasurfaces. *Sci. Adv.* https://doi.org/10.1126/sciadv.abg7488 (2021).
44. Rubin, N. A. et al. Matrix Fourier optics enables a compact full-Stokes polarization camera. *Science* https://doi.org/10.1126/science.aax1839 (2019).
45. Fienup, J. R. Phase retrieval algorithms: a comparison. *Appl. Opt.* **21**, 2758–2769 (1982).
46. Rubin, N. A. et al. Polarization state generation and measurement with a single metasurface. *Opt. Express* **26**, 21455–21478 (2018).
47. Arbabi, E., Kamali, S. M., Arbabi, A. & Faraon, A. Vectorial holograms with a dielectric metasurface: ultimate polarization pattern generation. *ACS Photon.* **6**, 2712–2718 (2019).
48. Rubin, N. A. et al. Imaging polarimetry through metasurface polarization gratings. *Opt. Express* **30**, 9389–9412 (2022).
49. Devlin, R. C., Khorasaninejad, M., Chen, W. T., Oh, J. & Capasso, F. Broadband high-efficiency dielectric metasurfaces for the visible spectrum. *Proc. Natl Acad. Sci. USA* **113**, 10473–10478 (2016).
50. Khorasaninejad, M. et al. Metalenses at visible wavelengths: diffraction-limited focusing and subwavelength resolution imaging. *Science* **352**, 1190–1194 (2016).
51. Li, L. W., Rubin, N. A., Juhl, M., Park, J.-S. & Capasso, F. Evaluation and characterization of imaging polarimetry through metasurface polarization gratings. *Appl. Opt.* **62**, 1704–1722 (2023).
52. Li, Q., Song, J., Alenin, A. S. & Tyo, J. S. Spectral–temporal channeled spectropolarimetry using deep-learning-based adaptive filtering. *Opt. Lett.* **46**, 4394–4397 (2021).
53. Yang, W. et al. Deep learning for single image super-resolution: a brief review. *IEEE Trans. Multimedia* **21**, 3106–3121 (2019).
54. Goto, A., Otomo, K. & Nemoto, T. Real-time polarization-resolved imaging of living tissues based on two-photon excitation spinning-disk confocal microscopy. *Front. Phys.* https://doi.org/10.3389/fphy.2019.00056 (2019).
55. Pahlevaninezhad, H. et al. Nano-optic endoscope for high-resolution optical coherence tomography in vivo. *Nat. Photon.* **12**, 540–547 (2018).
56. Qi, J. et al. Surgical polarimetric endoscopy for the detection of laryngeal cancer. *Nat. Biomed. Eng.* https://doi.org/10.1038/s41551-023-01018-0 (2023).
57. Oates, T. W. H., Shaykhutdinov, T., Wagner, T., Furchner, A. & Hinrichs, K. Mid-infrared gyrotropy in split-ring resonators measured by Mueller matrix ellipsometry. *Opt. Mater. Express* **4**, 2646 (2014).
58. Schmidt, D. Characterization of highly anisotropic three-dimensionally nanostructured surfaces. *Thin Solid Films* **571**, 364–370 (2014).
59. Heinzl, T. et al. On the observation of vacuum birefringence. *Opt. Commun.* **267**, 318–321 (2006).
60. Azzam, R. M. A. Three-dimensional polarization states of monochromatic light fields. *J. Opt. Soc. Am. A* **28**, 2279 (2011).
61. Marx, B. et al. High-precision X-ray polarimetry. *Phys. Rev. Lett.* https://doi.org/10.1103/physrevlett.110.254801 (2013).
62. Wiesauer, K. & Jördens, C. Recent advances in birefringence studies at THz frequencies. *J. Infrared Millim. Terahertz Waves* **34**, 663–681 (2013).

Methods

Phase retrieval optimization for structured polarization illumination

To generate the structured polarized illumination (equation (2)), we designed a computer-generated hologram. Recent studies on polarization metasurfaces[43,47] describe how to use conventional phase retrieval algorithms such as the Gerchberg–Saxton algorithm, to design computer-generated holograms for structured polarized light. We used the same principles to design the structured polarized light defined in equation (2).

We start by considering the electric field components (in the paraxial regime) just after the metasurface: $(E_x^{\text{meta}}, E_y^{\text{meta}})$. As the metasurface is phase only, the field right after the metasurface has unity amplitude—that is, $\sqrt{|E_x^{\text{meta}}|^2 + |E_y^{\text{meta}}|^2} = 1$. The electric field components in the far field, $(E_x^{\text{far}}, E_y^{\text{far}})$, are related to the electric field components right after the metasurface using Fourier optics. At the nth iteration we have:

$$\begin{aligned} E_x^{\text{meta}}(n) &= \frac{\mathcal{F}\{E_x^{\text{far}}(n)\}}{I(n)} \\ E_y^{\text{meta}}(n) &= \frac{\mathcal{F}\{E_y^{\text{far}}(n)\}}{I(n)} \\ I(n) &= \sqrt{|\mathcal{F}\{E_x^{\text{far}}(n)\}|^2 + |\mathcal{F}\{E_y^{\text{far}}(n)\}|^2} \end{aligned} \tag{6}$$

where the total amplitude $I(n)$ is used to normalize the field components, as the total field has unity amplitude. For the particular polarization distribution we want in the far field, we can define the target amplitudes $|E_x^{\text{targ}}|$, $|E_y^{\text{targ}}|$ and relative phase $\phi^{\text{targ}} = \angle E_y^{\text{targ}} - \angle E_x^{\text{targ}}$. For half of the total number of iterations, the fields are updated as:

$$\begin{aligned} E_x^{\text{far}}(n) &= |E_x^{\text{targ}}| \exp\left(i\angle\mathcal{F}\{E_x^{\text{meta}}(n-1)\}\right) \\ E_y^{\text{far}}(n) &= |E_y^{\text{targ}}| \exp\left(i\angle\mathcal{F}\{E_x^{\text{meta}}(n-1)\} + i\phi^{\text{targ}}\right) \end{aligned} \tag{7}$$

and for the remaining half, are updated as:

$$\begin{aligned} E_x^{\text{far}}(n) &= |E_x^{\text{targ}}| \exp\left(i\angle\mathcal{F}\{E_y^{\text{meta}}(n-1)\} - i\phi^{\text{targ}}\right) \\ E_y^{\text{far}}(n) &= |E_y^{\text{targ}}| \exp\left(i\angle\mathcal{F}\{E_y^{\text{meta}}(n-1)\}\right) \end{aligned} \tag{8}$$

which ensures that the update process is symmetric with respect to both the electric field components.

In our implementation, we set the total number of iterations to 50—although we found the optimization to converge in much fewer iterations. Once the optimized field components (E_x^{meta}, E_y^{meta}) are retrieved, the Jones matrix profile for the metasurface (assuming a certain incident polarization), and resultantly, the nanopillar dimensions and orientations, are computed using Jones calculus and eigenvalue decomposition[40]. The steps are summarized in Supplementary Algorithm 1 (Supplementary Section 2).

Gradient-descent optimization for full-Stokes imaging

To design metasurface diffraction gratings for full-Stokes imaging, we optimize the metasurface design using gradient-descent optimization. This two-dimensional periodic metasurface design includes, in 1 period, 12 nanopillars × 12 nanopillars, with phases $\phi_x(m, n)$, $\phi_y(m, n)$, and orientation $\theta(m, n)$, which are initially randomized. This means $12 \times 12 \times 3 = 432$ parameters will be optimized. (The actual metasurface is composed of hundreds of periods.) The Jones matrix profile of the metasurface is given by equation (1). Consider a set of diffraction orders G, whose Jones matrices we want to control. In our case, $G = \{(1, 0), (0, 1), (-1, 0), (0, -1)\}$, which is the set of first four on-axis diffraction orders. We design the Jones matrices in these diffraction orders to behave as analysers for four different polarizations of our choice. The Jones matrix response $\tilde{J}_{\text{far}}(k_m, k_n)$, in a given diffraction order (k_m, k_n), can be computed using the Fourier transform, $\tilde{J}_{\text{far}}(k_m, k_n) = \mathcal{F}\{J_{\text{meta}}(m, n)\}$. For a gradient-descent optimization, one needs to define a merit figure to optimize, and any accompanying constraints. In our case, we can define the merit figure and constraints as follows.

Merit figure: the average intensity in orders of interest should be maximized.

- Mathematically, we can define the merit figure $\eta = \sum_{(k_m,k_n)\in\{G\}} I_j^{(k_m,k_n)}$, where $I_j^{(k_m,k_n)}$ is the normalized optical power when the preferred polarization state $|\,\mathbf{j}_{(k_m,k_n)}\rangle$ is incident.
- $I_j^{(k_m,k_n)} = \langle\, \mathbf{j}_{(k_m,k_n)} | \tilde{J}_{\text{far}}^{\dagger}(k_m, k_n)\tilde{J}_{\text{far}}(k_m, k_n) \,|\, \mathbf{j}_{(k_m,k_n)}\rangle$.

Constraint 1: the Jones matrix response $\tilde{J}_{\text{far}}(k_m, k_n)$, for each order in G, should match the desired analyser response.

- Mathematically, we can write this as $\xi(k_m, k_n) = 1\ \forall\ (k_m, k_n) \in \{G\}$.
- The 'contrast' ξ is defined as $\xi_{(k_m,k_n)} = \frac{I_j^{(k_m,k_n)} - I_{j,\perp}^{(k_m,k_n)}}{I_j^{(k_m,k_n)} + I_{j,\perp}^{(k_m,k_n)}}$, where $I_{j,\perp}^{(k_m,k_n)}$ is the normalized optical power on order (k_m, k_n) when $\left|\,\mathbf{j}_{(m,n)}^{\perp}\right\rangle$—orthogonal to the preferred polarization—is incident.
- $I_{j,\perp}^{(m,n)} = \left\langle \mathbf{j}_{(m,n)}^{\perp} \middle| \tilde{J}_{(m,n)}^{\dagger} J_{(m,n)} \middle| \mathbf{j}_{(m,n)}^{\perp} \right\rangle$.

Constraint 2: orders should have equal amplitudes/intensities—that is, when unpolarized light is incident on the grating, the light beams diffracted in orders in G should have equal intensities.

- Mathematically, we can write this as $\sigma(\{I_j^{(k_m,k_n)}\}) = 0 \quad \forall \quad (k_m, k_n) \in \{G\}$, where σ denotes the standard deviation operator.

After defining the merit figure and constraints, we use the open-source gradient-descent optimizer available on Python in its scipy library. The results of the numerical optimization have been reported in our previous works[44,48]. We summarize the steps of the optimization in Supplementary Algorithm 2 (Supplementary Section 2).

Metasurface fabrication

Although the two metasurfaces—for structured light and full-Stokes imaging—are designed and optimized separately, they are both fabricated using the exact same recipe involving TiO_2, to function at a wavelength of 532 nm. TiO_2, at visible wavelengths, is a relatively high-index and transparent material, and thus fitting for our metasurface fabrication. In our recipe[49], which follows a 'bottom up' approach, the TiO_2 is deposited after patterning, as features are constructed atom by atom by atomic layer deposition (ALD). From the theoretical and numerical design to the final metasurface device, we follow specific steps involving nanofabrication in a controlled environment, as detailed below.

(1) Spin-coating the electron beam resist. Glass substrates are first coated with hexamethyldisilazane and then spin-coated with an undiluted positive-tone electron beam resist (ZEP-520A; Zeon Chemicals). We spin the resist at 1,750 rpm, following our spin curve, to achieve the desired thickness of 600 nm. The resist is then baked at 180 °C for 5 min.

(2) Electron beam lithography. We first deposit 10 nm of chromium via electron beam evaporation to avoid charging the sample during the writing process. For lithography, the patterns are exposed to an accelerating voltage of 125 kV and beam diameter of 2 nm, using the ELS-F125 (Elionix) high-speed, high-precision thermal field emission electron beam lithography system. Following electron beam exposure, samples are developed in *o*-xylene for 60 s under gentle agitation.

(3) ALD. The TiO_2 is deposited using ALD. For the ALD (Savannah, Cambridge Nanotech) of TiO_2 we use a two-pulse system of water and TDMAT precursor: a 0.2 s water pulse is followed by a 7 s delay, and a 0.4 s TDMAT pulse is followed by a 10 s delay.

The system is left under a continuous flow of N_2 carrier gas at a rate of 20 cm^3 min^{-1} and a temperature of 90 °C, maintained throughout the process. These settings result in an overall deposition rate of 0.7 nm per cycle. ALD conformally coats the gaps and the surface, thus resulting in extremely smooth side walls (post-processing).

(4) Reactive ion etching (RIE). The RIE (dry etch) is carried out on a Unaxis inductively coupled plasma RIE with a mixture of Cl_2 (3 cm^3 min^{-1}) and BCL_3 (8 cm^3 min^{-1}), at a pressure of 4 mtorr, inductively coupled plasma power of 400 W and substrate bias of 150 V. Etch rates are usually between 1.3 nm s^{-1} and 1.6 nm s^{-1}.

(5) Removing the electron beam resist. Finally, the samples are exposed to ultraviolet radiation and ozone, followed by soaking in Remover PG (MicroChem Corporation) for 24 h to completely remove the electron beam resist.

The scanning electron microscope (SEM) images for both metasurface 1 and metasurface 2 are shown in Extended Data Fig. 1.

Data availability

All data are available in the paper or Supplementary Information.

Acknowledgements

This material is based on work supported by the Air Force Office of Scientific Research (AFOSR) under grant number FA9550-21-1-0312 (F.C.), the Office of Naval Research (ONR) under grant number N00014-20-1-2450 (F.C.) and the National Aeronautics and Space Administration (NASA) under grant numbers 80NSSC21K0799 (F.C.) and 80NSSC20K0318 (F.C.). This work was performed in part at the Harvard University Center for Nanoscale Systems (CNS): a member of the National Nanotechnology Coordinated Infrastructure Network (NNCI), which is supported by the National Science Foundation under NSF award number ECCS-2025158.

Author contributions

A.Z. conceived the idea and developed the theory with inputs from N.A.R. and F.C. A.Z. designed and optimized the metasurfaces. M.L.M. and N.A.R. fabricated the metasurfaces with assistance from J.-S.P. N.A.R. and L.W.L. performed full-Stokes imaging calibration. A.Z. performed the experiments with assistance from A.H.D. A.Z. analysed the data. F.C. supervised the project. All authors contributed to the writing of the paper.

Competing interests

The authors declare no competing interests.

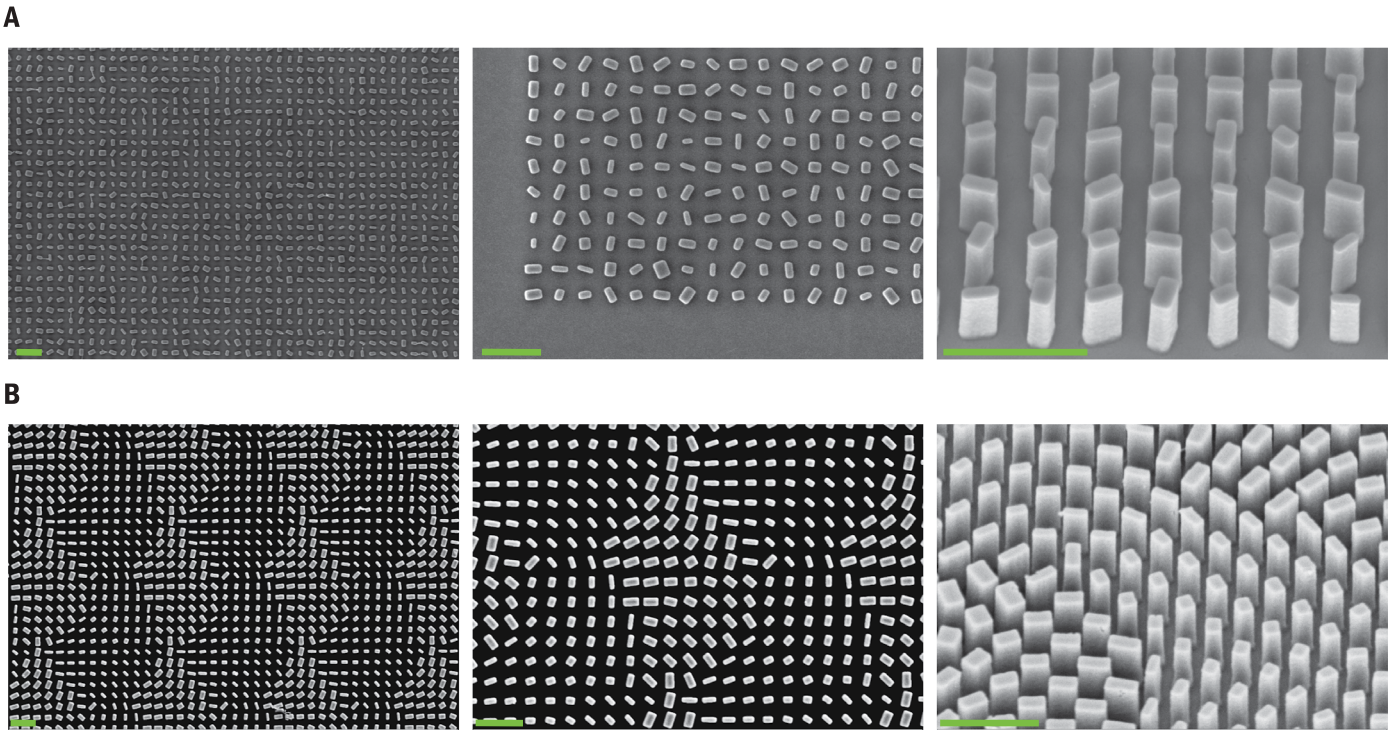

Extended Data Fig. 1 | SEM Images of Metasurfaces. (**A**) SEM images of the (aperiodic) metasurface hologram - Metasurface 1 - used to produce structured polarization illumination. (**B**) SEM images of the (periodic) metasurface diffraction grating - Metasurface 2 - used for full-Stokes imaging. (Scale bar: 1 μm).